

BEYOND THE MALTESE CROSS: GEOMETRY OF TURBULENCE BETWEEN 0.2 AND 1 AU

ANDREA VERDINI

UPMC, Paris, France
 Lesia, Observatoire de Paris, Meudon, France
 LPP, Ecole Polytechnique, Palaiseau, France

ROLAND GRAPPIN

LPP, Ecole Polytechnique, Palaiseau, France.
 (Dated: May 26, 2018)
 Draft version May 26, 2018

ABSTRACT

The spectral anisotropy of turbulent structures has been measured in the solar wind since 1990, relying on the assumption of axisymmetry about the mean magnetic field, B_0 . However, several works indicate that this hypothesis might be partially wrong, thus raising two questions: (i) is it correct to interpret measurements at 1 AU (the so-called Maltese cross) in term of a sum of slab and 2D turbulence? (ii) what information is really contained in the Maltese cross?

We solve direct numerical simulations of the MHD equations including the transverse stretching exerted by the solar wind flow and study the genuine 3D anisotropy of turbulence as well as that one resulting from the assumption of axisymmetry about B_0 .

We show that the evolution of the turbulent spectrum from 0.2 to 1 AU depends strongly on its initial anisotropy. An axisymmetric spectrum with respect to B_0 keeps its axisymmetry, i.e., resists stretching perpendicular to radial, while an isotropic spectrum becomes essentially axisymmetric with respect to the radial direction.

We conclude that close to the Sun, slow-wind turbulence has a spectrum that is axisymmetric around B_0 and the measured 2D component at 1 AU describes the real shape of turbulent structures. On the contrary, fast-wind turbulence has a more isotropic spectrum at the source and becomes radially symmetric at 1 AU. Such structure is hidden by the symmetrization applied to the data that instead returns a slab geometry.

Subject headings: Magnetohydrodynamics (MHD) — plasmas — turbulence — solar wind

1. INTRODUCTION

In a pioneering paper, Matthaeus et al. (1990) obtained for the first time an average picture of the turbulent structures in the solar wind by computing the autocorrelation of the interplanetary magnetic field fluctuations in different directions with respect to the mean field (B_0). and assuming axisymmetry about B_0 . Considering that single spacecraft measurements allow only to explore the radial structure of the fluctuations, obtaining the Maltese cross was a big progress, as it revealed the multidimensional structure of turbulence. The two-dimensional (2D) autocorrelation was made up of two lobes, one elongated along increments parallel to mean field, and the other elongated along increments perpendicular to it (hence the term “Maltese cross”). This particular shape was interpreted in terms of a mixture of 2D fluctuations with wavevectors and fluctuations perpendicular to the mean field (2D component), and of waves with wavevectors parallel to it (slab component), respectively.

The hypothesis of axisymmetry about B_0 underlying the Maltese cross picture is fully justified for homogeneous turbulence by theoretical, experimental and numerical results (Montgomery & Turner 1981; Shebalin et al. 1983; Grappin 1986) which all indicate that the nonlinear cascade leading to a turbulent spectrum proceeds mainly in directions perpendicular to the mean magnetic field. However, in the solar wind, the mean field direction is not the only symmetry axis for turbulent structures. Theoretical and numerical evidence (Völk & Aplers 1973; Grappin et al. 1993; Grappin & Velli 1996; Dong et al. 2014) indicate that the flow direction, i.e.

the radial axis, also plays a role in shaping the symmetry of the turbulent spectrum in the Fourier space. Also, for fluctuations with frequencies between 3 and 10 hours Saur & Bieber (1999) found that the best theoretical model fitting solar wind data is a mixture of 2D turbulence with wavevectors lying in a plane perpendicular to the mean field and a spectrum of wavevectors aligned with the radial, not aligned with the mean field.

The argument that explains why the radial axis also plays a role is simple: as a plasma volume is advected by the solar wind, the large scale flow cannot be eliminated by a Galilean transformation, because it is *radial, not uniform*. Indeed, after such a transformation, there remains an expanding flow transverse to the radial that leads to a transverse stretching of the plasma volume: this stretching has several consequences, an important one being that it slows down nonlinear coupling, at least in directions perpendicular to the radial. In principle, at small enough scales the axisymmetry about B_0 should be valid, since nonlinear couplings should overcome the transverse stretching: in fact their time scale becomes smaller while the expansion time scale is scale-independent. However, we will see in this paper that the situation is less simple and that the radial symmetry can prevail even at small scales.

More specifically, this paper aims at understanding when the hypothesis of axisymmetry about B_0 and the associated Maltese cross picture are valid or not, and, at the same time, at guessing the true initial properties of turbulence close to the Sun that could lead to the structures observed at 1 AU. We shall use for that the expanding box model (EBM

(Grappin et al. 1993)), which consists in magnetohydrodynamic (MHD) equations modified to include the effect of the large scale radial flow of the wind. The EBM equations describe the evolution of a plasma parcel advected by a radial, uniform radial wind. Its conditions of validity are the following: (i) the angular width of the plasma volume must be small in order to allow neglecting curvature terms (but see however Grappin & Velli (1996)); (ii) the radial extent of the domain must be small enough to allow assuming homogeneity within the domain; (iii) heliocentric distance must be larger than, say, 0.1 AU to be able to neglect systematic large-scale variations of the solar wind speed with heliocentric distance. The EBM equations have been used recently with success (Verdini & Grappin 2015) to reproduce and fully explain the local anisotropy of turbulent structures measured in the solar wind by Chen et al. (2012). The term *local* means that the anisotropy is measured in a frame attached to the *local* mean magnetic field that varies both with scale and location. Note, however, that *local* anisotropy is not easily related to the standard anisotropy studied in the present paper that is defined in a fixed frame, independent of scale (see Matthaeus et al. (2012)).

In a previous work, Ghosh et al. (1998) attempted to reproduce the Maltese cross via direct numerical simulations of MHD equations, thus without taking into account the large scale radial flow of the wind. Using the hypothesis of axisymmetry about B_0 , they were able to find separately the two lobes by varying the initial conditions of their runs. They obtained the 2D component for initial conditions corresponding to 2D turbulence or to pressure balance structures (Carbone et al. 1995), and the slab component for initial conditions corresponding to unidirectional Alfvén waves with wavevectors quasi-parallel to the magnetic field. However a mixture of these initial conditions led to isotropic autocorrelation, so they concluded that the two lobes of the Maltese cross result from a mixture of different solar wind states. This is indeed the case, as was shown by Dasso et al. (2005) and subsequent works (Hamilton et al. 2008; Weygand et al. 2009, 2011), which successfully isolated the slab component and the 2D component by partitioning the fluctuations in fast and slow streams, respectively.

Our purpose here is twofold: (i) to propose a description of the possible properties of turbulence close to the Sun compatible with these observations at 1 AU; (ii) explain how the hypothesis of axisymmetry about B_0 transforms this turbulence into the classical (2D, slab) model. An extreme example of such a transformation is provided in fig. 1 which represents the effect of symmetrization around B_0 on a turbulent spectrum with radial symmetry, that is, an anisotropy completely ruled by expansion¹. The projection in the ecliptic plane of the 3D spectrum with radial symmetry is shown in panel (a). By averaging around the mean field direction, we obtain successively the panels (b) and (c). This is equivalent to applying the hypothesis of axisymmetry about B_0 to measurements that belong to several samples with different angles of the mean field with respect to the radial. Panel (d) represents the last step, i.e. the spectrum rotated in the frame associated with the mean field. The final spectrum has two properties: (i) by construction, it is axisymmetric with respect to the mean field, while the true spectrum is axisymmetric with respect to the radial; (ii) it has a complicated structure with main excita-

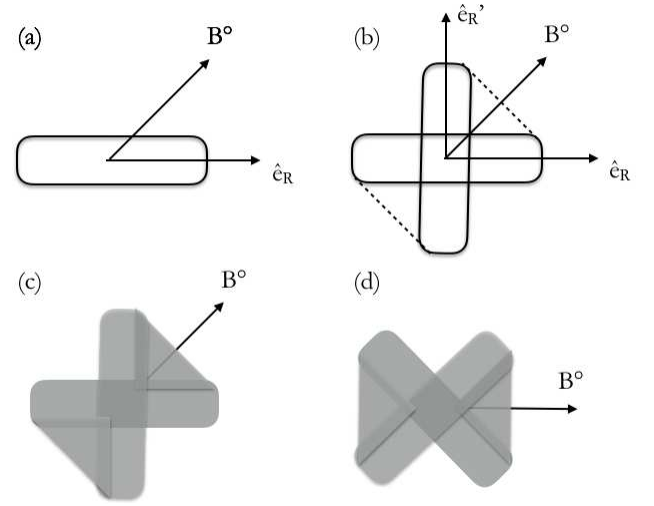


FIG. 1.— Symmetrization around B_0 of a spectrum axisymmetric with respect to the radial direction, with the mean field B_0 at an angle $\pi/4$ with the radial. (a) projection on the (B_0, e_R) plane of an isocontour of the 3D spectrum that is axisymmetric around the radial direction; (b) applying to the isocontour the assumption of axisymmetry about B_0 ; (c) filling the interior of the contour to give an idea of the new symmetrized spectrum; (d) rotating the cartesian frame, with the x axis aligned with the mean field B_0 as done when presenting the Maltese cross.

tion along the mean field (i.e. the observed slab component), which masks the true (physical) structure of the spectrum.

To reveal the possible initial structure and evolution of the (2D, radial slab) two-component turbulence of Saur & Bieber (1999), we follow in this paper the evolution of a plasma volume advected by the wind from 0.2 AU to 1 AU (fig. 2), using the EBM equations. The EBM equations have been used in Dong et al. (2014) to explain basic properties of solar wind turbulence, namely the anisotropy of the different components of fluctuations, both kinetic and magnetic (also termed variance anisotropy). The present work extends this study by varying (i) the initial conditions at 0.2 AU; (ii) the ratio between the nonlinear turnover time based on the largest eddies and the linear stretching time.

The plan of the paper is as follows. Simulations and parameters are described in Section 2. Results on the anisotropy of solar wind turbulence and its appearance in data under the assumption of axisymmetry about the mean field are given in Section 3. In section 4 we present a discussion on the results and the impact of initial spectra and expansion parameter on anisotropy. The last section contains the conclusions.

2. SIMULATIONS AND PARAMETERS

The list of runs is indicated in Table 1 along with the main parameters. We now explain the different parameters.

2.1. Expansion parameter ϵ , time and distance

In a plasma volume advected by the radial wind, the linear stretching of the volume in directions perpendicular to the *radial* transfers energy to *larger scales* (fig. 2). On the other hand, the nonlinear couplings transfer energy to *smaller scales* in directions perpendicular to the *mean field*. The relative strength of these different tendencies is quantified by the *expansion parameter*, ϵ , which is the ratio of the nonlinear

¹ We consider the 3D spectrum instead of the 3D autocorrelation because rotating and averaging are more easily visualized in the Fourier space

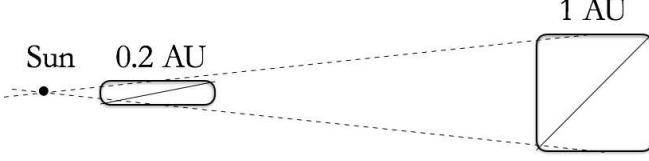


FIG. 2.— Initial and final domains of simulation (and plasma volume as well) in the ecliptic plane. Thin lines: direction of mean magnetic field. For all runs with expansion, the aspect ratio of the domain varies from 1/5 to unity, and the mean magnetic field angle with the radial varies from $\tan^{-1}(1/5)$ to $\tan^{-1}(1) = \pi/4$.

time $t_{NL} = 1/(k_0 u)$ and the expansion time $t_e = R/U_0$:

$$\epsilon = t_{NL}/t_e = (U_0/R)/(k_0 u) \quad (1)$$

where U_0 is the (constant) wind speed, R the heliocentric distance of the plasma volume, k_0 the minimum wavenumber associated with the dimension transverse (to radial) of the plasma volume, and u the initial rms amplitude of the velocity fluctuations. Except if otherwise stated, the expansion parameter will be evaluated at the initial distance R_0 : this is an important control parameter of each run. Remark that the expansion parameter is not necessarily constant with time. In Table 1, we give both the initial value, ϵ , and the value evaluated at the end of the run, ϵ_{end} : as one can see it increases for all runs.

A given run will be characterized by (i) the detailed initial conditions (see end of Section); (ii) the initial expansion parameter ϵ . Since the nonlinear couplings increase at small scales while the expansion effect is scale-independent, one expects that for a given expansion rate ϵ of order unity the wavenumber range is made of two subsets: the larger scales are dominated by the linear effect of expansion, while the smaller scales are dominated by nonlinear effects (Dong et al. 2014). However, we will find that the existence and location of such ranges depend largely on the anisotropy of the initial spectrum, and this will be a basic result of the paper.

As time increases, the heliocentric distance increases as:

$$R = R_0 + U_0 t \quad (2)$$

or, measuring time in terms of the initial nonlinear time:

$$R/R_0 = 1 + \epsilon t \quad (3)$$

All expanding runs have $R_{max} = 5R_0$, allowing us to follow the evolution of the plasma between 0.2 and 1 AU, as stated in the introduction.

2.2. Initial physical parameters

The initial magnetic and kinetic fluctuations are solenoidal, obtained as a sum of random-phase modes, and are at equipartition with root-mean-square value equal to one, $b_{rms} = u_{rms} = 1$. Density and temperature are uniform; density is unity, sound speed is $c_s \sim 8$, so that the initial Mach number of the fluctuations $M = u_{rms}/c_s = 0.12$ and remains small, as well as the relative amplitude of the compressible component.

2.3. Resolution, simulation domain and mean magnetic field

The evolution of a turbulent spectrum in the solar wind is studied by integrating the EBM equations with given initial conditions (decaying simulations). The resolution is $N_x = N_y = N_z = 512$. Except for the single homogeneous run A

TABLE 1

LIST OF RUNS AND THEIR PARAMETERS. ALL RUNS HAVE INITIALLY $b_{rms} = u_{rms} = 1$, DENSITY UNITY, AND END UP WITH A DOMAIN OF UNIT ASPECT RATIO AND A MEAN MAGNETIC FIELD B_0 AT 45° WITH THE RADIAL (x). I.C. COLUMN: QUALIFIES THE INITIAL SPECTRUM, EITHER “B₀-AXISYMMETRIC” IF AXISYMMETRIC WITH RESPECT TO B_0 , OR “ISO” IF ISOTROPIC. k_y^{cut} IS THE MAXIMUM VERTICAL EXTENT OF THE INITIAL k^{-1} SPECTRUM (FOR RUNS WITH EXPANSION). IN THE COLUMN B_0 WE INDICATE THE x AND y COMPONENTS OF THE INITIAL MEAN MAGNETIC FIELD. χ IS A MEASURE OF THE STRENGTH OF TURBULENCE BASED ON INITIAL CONDITIONS (SEE EQ. 4 AND THE CORRESPONDING TEXT). ϵ IS THE INITIAL EXPANSION PARAMETER. ϵ_{end} IS THE FINAL EXPANSION PARAMETER. t_{end} IS THE END TIME, IN NONLINEAR TIME UNITS. ALL EXPANDING RUNS HAVE $R/R_0 = 5$ WHERE R_0 , R ARE THE INITIAL AND FINAL HELIOCENTRIC DISTANCES, RESPECTIVELY. b_{rms}/B_0 IS THE RATIO BETWEEN THE RMS AND MEAN MAGNETIC FIELD AT THE END OF THE SIMULATION.

Run	I.C.	k_y^{cut}	B_0	χ	ϵ	ϵ_{end}	t_{end}	b_{rms}/B_0
A	B ₀ Axis		$(\sqrt{2}, \sqrt{2})/2$	4	0	0	4	0.8
B	B ₀ Axis	128	$(2, 2/5)$	2.5	0.4	1.1	10	0.6
C	ISO	128	$(2, 2/5)$	1.2	0.4	1.1	10	0.6
D1	B ₀ Axis	64	$(2, 2/5)$	2.5	0.4	0.97	10	0.5
D2	B ₀ Axis	64	$(2, 2/5)$	2.5	1	1.9	4	0.5
D3	B ₀ Axis	64	$(2, 2/5)$	2.5	2	3.3	2	0.5
D4	B ₀ Axis	64	$(2, 2/5)$	2.5	3	4.8	4/3	0.5
D5	B ₀ Axis	64	$(2, 2/5)$	2.5	4	6.2	1	0.5
E1	ISO	64	$(2, 2/5)$	0.6	0.1	0.26	40	0.6
E2	ISO	64	$(2, 2/5)$	0.6	0.2	0.51	20	0.7
E3	ISO	64	$(2, 2/5)$	0.6	0.4	1.0	10	0.5
E4	ISO	64	$(2, 2/5)$	0.6	1	1.6	4	0.5
E5	ISO	64	$(2, 2/5)$	0.6	2	2.8	2	0.5

with zero expansion ($\epsilon = 0$), for all other runs the domain is expanding in the directions y and z perpendicular to the radial (x).

The *non-expanding* run A has an initial domain which is a cube with sizes $L_x = L_y = L_z = 2\pi$, and mean magnetic field $B_0 = (1/\sqrt{2}, 1/\sqrt{2})$ in the xOy plane.

The *expanding* runs have an initial domain elongated by a factor 5 in the radial direction: $L_x = 5L_y = 5L_z = 5 \times 2\pi$. In doing so, we anticipate the stretching perpendicular to the radial, which transforms the domain into a cube at the distance $R = 5R_0$. Remark that one could start with a cubic domain as well, and thus end up with a domain stretched in the directions perpendicular to radial (this was the choice adopted in Dong et al. 2014). We prefer to end up with a cubic domain because (i) we are mostly interested in the turbulent state close to 1 AU; (ii) we think that nonlinear interactions are essentially local. In this way we hope to better catch the properties of the turbulent cascade at the end of the simulation.

The initial mean magnetic field makes a small angle with the radial: $B_0 = (2, 2/5)$. As the distance increases by a factor 5, the mean magnetic field rotates due to magnetic flux conservation and makes an angle of 45° with the radial at the end of the simulation (see fig. 2).

2.4. Initial spectrum

For the homogeneous run A, we consider a bi-gaussian spectrum of the form $\exp[-(k_\perp/2\Delta k_\perp)^2 - (k_\parallel/2\Delta k_\parallel)^2]$ with a larger width in directions perpendicular to the mean field, $\Delta k_\perp = 4\Delta k_\parallel = 4$. Note that changing the precise ratio, e.g., taking an isotropic initial spectrum, does not change the results at times longer than a couple of nonlinear times.

We now describe expanding runs. We consider as in Dong et al. (2014) an initial fluctuation spectrum at equipartition between magnetic and kinetic fluctuations, with a 1D k^{-1} scaling, thus mimicking the fossil part of the spectrum measured in the fast streams. It is convenient as well to use such

a strong small-scale excitation because otherwise, when only large scales are present initially, a too large expansion parameter prevents the direct cascade to form (Dong et al. 2014).

We consider two variants of the k^{-1} spectrum in figs. 3b,c. First, we consider (panel b) energy isocontours elongated in the radial direction, with an aspect ratio of 5, thus following the shape of the initial domain in Fourier space (dashed lines), which is opposite to that in real space (fig. 2). As in expanding runs the initial mean field forms a small angle with the radial ($\tan^{-1}(1/5)$), this spectrum is approximately axisymmetric with respect to B_0 with an aspect ratio roughly corresponding to a critical balance condition (we checked that choosing true or approximate axisymmetry does not affect the results presented here). Runs starting with such spectra are denoted by “B₀Axis” in Table 1, and in the text “B₀-axisymmetric”. This term will denote at the same time axisymmetry with respect to the mean field and a spectrum principal axis perpendicular to B_0 . Of course, this property is not necessarily conserved with time.

Second, we considered energy isocontours with aspect ratio unity, thus not following the shape of the initial plasma volume (see fig. 3c). Such runs are denoted by “ISO” in Table 1, and in the text “isotropic”. Again, this property is not necessarily conserved with time.

The k^{-1} spectrum is cut to zero for $k_{y,z} \geq k_y^{cut}$ (the value is 128 or 64 depending on the run, see Table 1). The aspect ratio of the truncation in wavevector space follows the aspect ratio of the isocontours (isotropic or B₀-axisymmetric). Note that in practice, the *isotropic* spectrum of run C is truncated in the radial direction (x) by the domain boundary, not by the truncation wavenumber k_y^{cut} (see figs. 3b-c, in which the domain boundaries are indicated by dashed horizontal and vertical lines). On the contrary, for the class of isotropic runs E_{1...5} the truncation is at a smaller wavenumber and the spectrum is almost truly isotropic (their initial conditions are represented by the three inner circles in fig. 3c). In table 1 we also indicate the parameter

$$\chi = B_0 k_{\parallel}^{cut} / b_{rms} k_{\perp}^{cut}, \quad (4)$$

with k_{\perp}^{cut} and k_{\parallel}^{cut} indicating the maximal wavenumber excited in the direction perpendicular and parallel to the mean field respectively (for expanding runs $k_{\perp}^{cut} \sim k_y^{cut}$ and $k_{\parallel}^{cut} \sim k_x^{cut}$). This parameter complements the information on the symmetry of the spectrum since it quantifies the strength of turbulence as the ratio of the smallest Alfvén time to the smallest nonlinear time associated with initial conditions². As a rule, all B₀-axisymmetric runs have initially strong turbulence ($\chi > 1$), while isotropic runs have weak turbulence ($\chi < 1$). The only exception is run C that has $\chi \sim 1$ due to the truncation by the domain boundary.

3. RESULTS

We focus in this section on the first three runs of Table 1: run A without expansion and B₀-axisymmetric initial conditions, run B with expansion and B₀-axisymmetric initial conditions, run C with expansion and isotropic initial conditions. Our analysis of the magnetic structure of each run will follow the following steps.

First we represent 3D magnetic spectra at 0.2 and 1 AU with some detail in order to reveal the true evolution of anisotropy.

² The same parameter was used in forced simulations to induce weak or strong turbulence regimes (Dmitruk & Gómez 1999; Rappazzo et al. 2007; Perez & Boldyrev 2008; Verdini & Grappin 2012)

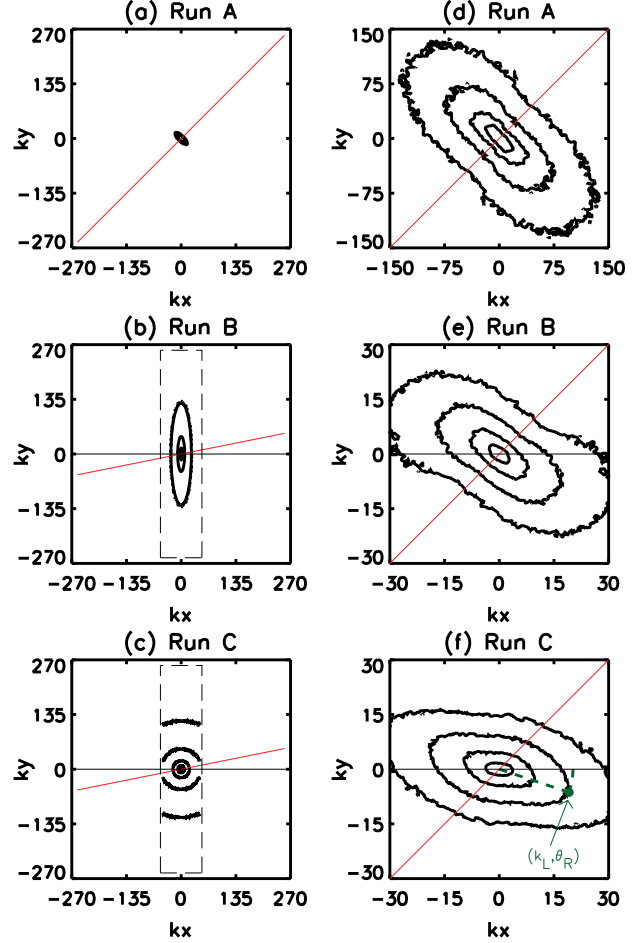


FIG. 3.— Isocontours of the 3D magnetic energy spectrum in the (k_x, k_y) plane, i.e., for $k_z = 0$ for Runs A, B and C. Left panels, at $t = 0$; right panels at the end of the simulation (see Table 1). The oblique red line indicates the mean magnetic field direction. In panels (b) and (c) the Fourier domain at the initial distance $R = R_0 = 0.2$ AU is bounded by the dashed horizontal and vertical lines. In panels (e) and (f) only a part of the Fourier domain is shown at the final distance of $R = 1$ AU (the true extent is $[-51.2, 51.2]^2$ with minimum wavenumber 0.2). In panel (f) we illustrate the measure of the anisotropy that is used to construct fig. 7: the filled dot indicated by the arrow marks the maximal distance of a given isocontour level from the center in the polar coordinates (k_L, θ_R) .

Second we draw “B₀-symmetrized” 3D spectra, obtained by averaging the 3D spectrum over the azimuthal angle around the mean magnetic field axis,

$$E_{3D}(k_{\parallel}, k_{\perp}) = 1/2\pi \int E_{3D}(k_{\parallel}, k_{\perp}, \phi) d\phi, \quad (5)$$

in order to understand how much this procedure reveals or hides details about the true 3D spectra.

Third, we transform the B₀-axisymmetric 3D spectrum into the 2D autocorrelation,

$$A(\ell_{\parallel}, \ell_{\perp}) = \int E_{3D} k_{\perp} \exp[i(k_{\parallel} \ell_{\parallel} + k_{\perp} \ell_{\perp})] dk_{\parallel} dk_{\perp}, \quad (6)$$

to make a link between our simulations and the observed solar wind structures (the Maltese cross).

In this Section, the role of initial conditions is analyzed in runs B and C, at a fixed expansion parameter, with Run A (zero expansion) playing the role of a test simulation. The

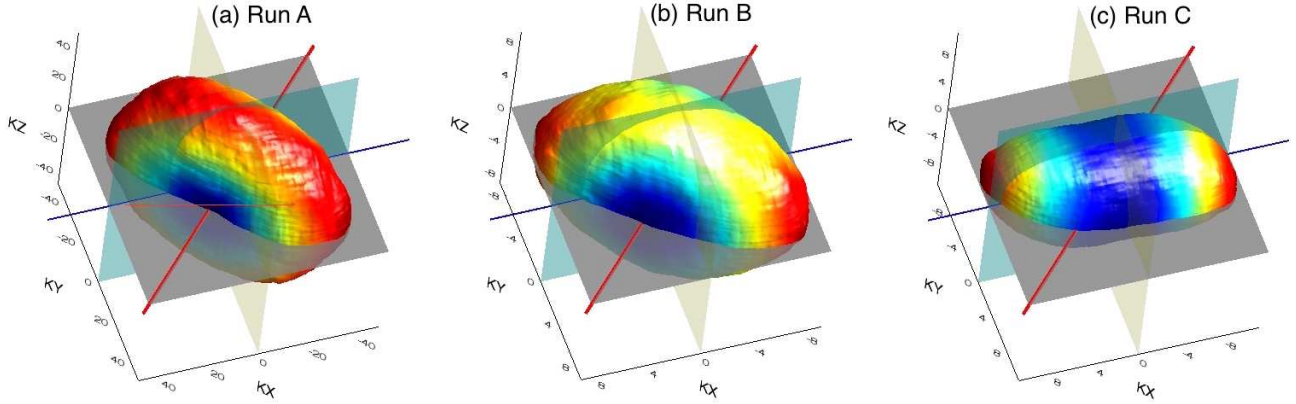


FIG. 4.— Runs A, B, C. Representative isosurface in the inertial range of the 3D magnetic energy spectrum at 1 AU (end of each run, cf. Table 1). Color indicates the distance to origin and is meant to give redundant information on the shape of the isosurface.

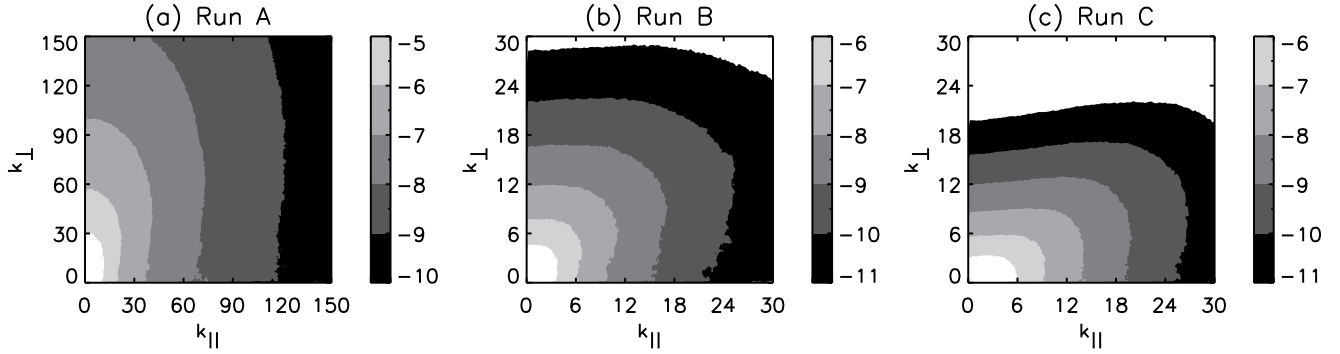


FIG. 5.— Run A, B, C at the end of the simulation (see Table 1). 3D spectra, after symmetrization around the mean magnetic field, in the frame attached to the mean field (k_{\parallel} , k_{\perp}) indicate the axis parallel and perpendicular to the mean field, respectively.

role of the expansion parameter ϵ is analyzed later in the Discussion with runs D_{1...5} and E_{1...5}.

3.1. The 3D structure

In the right panels of Figure 3 we show isocontours of the *ecliptic* cut (i.e., $k_z = 0$) of the 3D spectra after four nonlinear times for run A, and ten nonlinear times for runs B and C (thus at $R = 1$ AU). The mean magnetic field is indicated by a red line, which has an angle $\pi/4$ with the radial direction (k_x , black line). One sees that for run A the cascade proceeds perpendicularly to the mean field. For run B, this is about true, with a small deviation in the radial direction. For run C, the isocontours show an equal amount of stretching towards the radial direction and the field-perpendicular direction. Note that runs B and C develop a 1D spectrum with scaling close to $k^{-5/3}$ in the subrange $1 \leq k \leq 10$ (not shown)

The ecliptic view is complemented by fig. 4 where we show a 3D perspective of one representative isosurface of the spectrum taken in the inertial range, for the three runs A, B, and C. Colors give the distance to the origin as a redundant information. The red diagonal line is the B_0 direction, the blue line indicates the radial k_x direction. Again, the two runs A and B appear to both exhibit axisymmetry with respect to B_0 (with a cascade perpendicular to it), while run C shows a dominant radial axisymmetry, with what resembles a cascade along the radial. Note that for run B not only is the symmetry axis slightly tilted with respect to the mean field but also axisymmetry is

only roughly established (the isosurface is less elongated in the k_z direction than in the perpendicular direction lying in the ecliptic plane, $k_z = 0$).

3.2. Symmetrization around the mean field

We now use “blindly” the hypothesis of axisymmetry about B_0 , that is, we average all 3D spectra on the azimuthal angle around the mean field. The result is shown in fig. 5. The dominant symmetry of the spectrum is respected for run A, in a mild way for run B, not at all for run C. Indeed, the cascade is perpendicular to B_0 for run A. For run B, the deviation from B_0 -axisymmetry is large enough, so that the symmetrization transforms the spectrum into a quasi-isotropic spectrum. For run C, the deviation from B_0 -axisymmetry is so large that the symmetrization leads to a spectrum elongated along the direction *parallel to the mean field*.

The last step consists in transforming the averaged 3D spectra into 2D spectra by integrating, and then taking the Fourier transform to recover the 2D correlation figures, allowing comparison with 2D-autocorrelation of solar wind data. The result is shown in fig. 6. Run A has a 2D-correlation elongated in the parallel direction. Run B has a smaller elongation but still in the parallel direction while run C has its correlation elongated in the perpendicular direction. These last two opposite elongations are strongly reminiscent of the two figures obtained by the analysis of respectively slow and fast winds by Dasso et al. (2005) that correspond to the two lobes of the

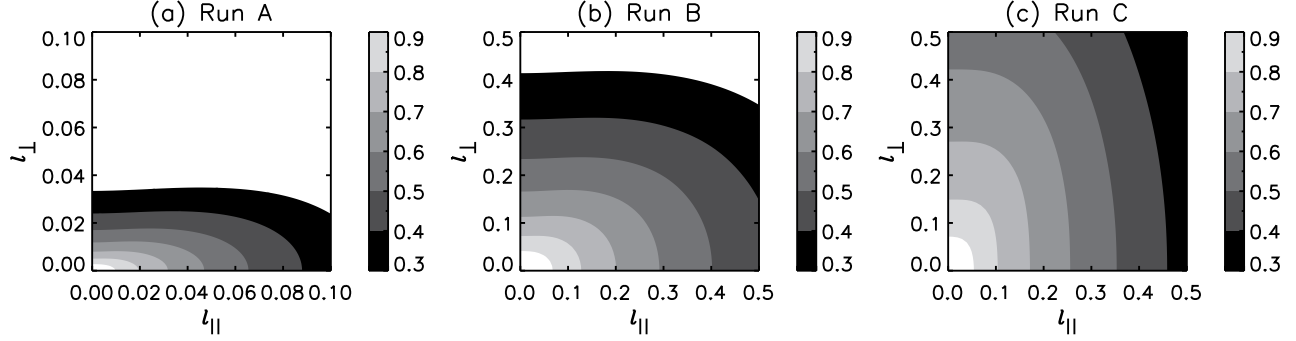


FIG. 6.— Run A, B, C at the end of the simulation (see Table 1). 2D autocorrelation obtained from the B_0 -axisymmetric 3D spectra of fig. 5 ($\ell_{||}$, ℓ_{\perp} indicate increments parallel and perpendicular to the mean field, respectively).

Maltese cross (in which fast and slow wind are mixed).

4. DISCUSSION

4.1. The 3D anisotropy and the Maltese cross

We have examined three runs, run A with no expansion, two runs with the same expansion rate but different initial conditions: a B_0 -axisymmetric and anisotropic spectrum (run B) and an isotropic spectrum (run C). We have two kinds of conclusions dealing respectively with the true structure of turbulence and with its *apparent* structure, i.e., after symmetrization around B_0 .

About the true structure of turbulence. Without expansion the end-result is *always* that the spectrum is elongated in directions perpendicular to the mean field (Montgomery & Turner 1981; Shebalin et al. 1983; Grappin 1986). However, with expansion, the conclusion is different: the “end” result depends strongly on the initial condition, as we have seen: the “perpendicular” cascade is not an attractor, or at least it is a weak attractor.

About the symmetrized structure, namely the 2D-correlation. In absence of expansion it captures the true 3D anisotropy, as expected. In presence of expansion, initial conditions “perpendicular to mean field” transform into itself, that is the so-called 2D turbulence. In fact the true 3D anisotropy is roughly axisymmetric with a symmetry axis close to the mean field direction, so that the 2D correlation returns qualitatively the correct anisotropy. With expansion still, “isotropic” initial conditions transform into the typical figure of the so-called “slab” turbulence, with isocontour elongated in the direction parallel to the mean field. In fact, because the true symmetry axis is along the radial direction, the symmetrization changes qualitatively the autocorrelation, as represented in Figure 1, ultimately transforming it from slab along the radial direction into slab along the mean-field direction.

In view of the observed association between (i) fast winds and slab signature; (ii) slow winds and 2D signature, it is thus tempting to propose that turbulence at the source of fast winds has an isotropic spectrum, and turbulence at the source of slow winds has an anisotropic spectrum with a cascade perpendicular to the mean field. We will come back to this point in the conclusions.

4.2. Anisotropy scaling and expansion rate

The simplicity of the symmetrized figures (figs. 5-6) is in contrast with the more complex real 3D structure - and the physics that is really at work. It not only gives a false im-

pression of the real symmetries, but it also suggests that the anisotropy is scale-independent, which, strictly, cannot be true - and is not true. Indeed, the expansion timescale is independent of scale, while the nonlinear timescale and the relative fluctuations’ amplitude, b_k/B_0 , decrease with scale. Since the latter two control the amount of anisotropy with respect to the mean field, we also expect the anisotropy to depend on scale. Indeed, if we look at fig. 3f (run C, isotropic initial conditions), one sees that the actual symmetry axis changes systematically when going from large scales to small scales.

Thus, varying the expansion parameter should allow us to vary the extent of the scales dominated by expansion and those dominated by nonlinear couplings. We now consider the two series of runs, runs $D_{1...5}$ and $E_{1...5}$ with increasing expansion parameter ϵ and different initial condition (B_0 -axisymmetric and isotropic, respectively). To describe the change of anisotropy with scale in a given run, we measure for each isocontour of the 2D ecliptic spectrum the maximal distance from the origin $k_L = \sqrt{k_x^2 + k_y^2}$ and the corresponding angle with respect to the radial direction θ_R (an illustration of the method is given in fig. 3f). The result is shown in fig. 7a for runs with B_0 -axisymmetric initial conditions, and in fig. 7b for runs with isotropic initial conditions (see Table 1). Note that for run A, k_L is renormalized by a factor 5, in order to allow compare run A without expansion with runs with expansion which have different domain sizes (see fig. 3).

Consider first the series, $D_{1...5}$, with B_0 -axisymmetric initial conditions and decreasing ϵ , fig. 7a. In absence of expansion the standard perpendicular cascade (that is, perpendicular to B_0) is well measured by the method, with $\theta_R \sim -45^\circ$ at small enough scales (solid line). With expansion, the principal-axis angle θ_R slightly decreases with k . For large k and large expansion parameter it is clustered around -37° and it approaches -42° at the smallest expansion parameter $\epsilon = 0.2$, that is the B_0 -anisotropy. This suggests that the B_0 -axisymmetry is an attractor at small scales for turbulence in the expanding solar wind (recall that smaller expansion parameters correspond roughly to smaller scales for given solar wind speed and fluctuations’ amplitude, see the definition of ϵ in eq. (1)).

Consider now the series of runs $E_{1...5}$ with isotropic initial conditions, fig. 7b. With expansion, all angles θ_R systematically decrease with k , with possibly a common asymptote at -34° as indicated by runs with $\epsilon \in [0.1, 0.4]$. Whether the true asymptote is the B_0 -anisotropy (i.e., $\theta_R = -45^\circ$) or an intermediate value, as suggested by the figure, is to be proven

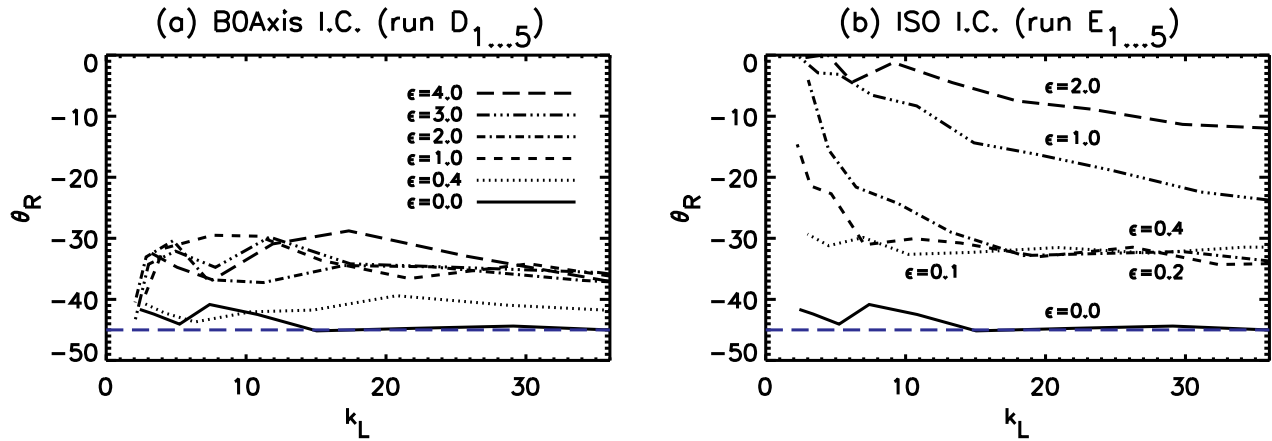


FIG. 7.— Angle θ_R between the largest axis of isocontours and the radial direction versus the lengths of the largest axis k_L for different levels of isocontours (see fig. 3f for an example). (a) Runs $D_{1...5}$ (B_0 -axisymmetric initial conditions); (b) Runs $E_{1...5}$ (isotropic initial conditions). The long-dashed line is the expected B_0 -anisotropy at -45° . The case of run A with $\epsilon = 0$ (solid line) is added on both panels, with abscissa renormalized by a factor 5, thus taking into account the different domain sizes (see fig. 3).

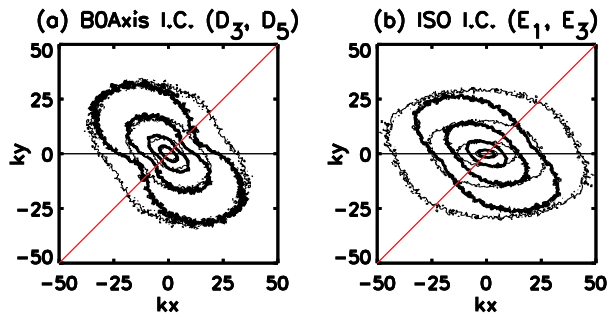


FIG. 8.— Superposition of final 2D isocontours (ecliptic cuts, $k_z = 0$) for two values of ϵ : 0.4 (thick lines) and 2 (thin lines). (a) B_0 -axisymmetric initial conditions; (b) isotropic initial conditions.

with simulations made at much larger Reynolds numbers.

Whatever the true asymptotic value, the important result is that, with reasonable values of ϵ_{end} at 1 AU, that is between 0.3 and 2 (Grappin et al. 1991), the first decade of the inertial range has an anisotropy that is strongly influenced by expansion since the symmetry axis is determined by *both* the radial and the mean-field direction.

The insensitivity to expansion of the runs with B_0 -axisymmetric initial conditions compared to isotropic initial conditions is illustrated in fig. 8. We overplot in each case the isocontours of two runs with $\epsilon = 0.2$ (thick lines) and $\epsilon = 2$ (thin lines). For B_0 -axisymmetric initial conditions the final contours are almost superposed, while with isotropic initial conditions the final contours vary strongly with ϵ : the isocontours with large ϵ are almost isotropic (actually compatible with $\theta_R \simeq 0$), while with small ϵ they are rather close to the isocontours with initial B_0 -axisymmetry.

When expansion matters, as in the case of isotropic spectra, the final anisotropy keeps trace of the particular initial spectrum. Consider run C in fig. 3f and run E_1 in fig. 8b (thick lines), which differ only by the value of the cut in the initial spectrum, $k_{cut}^y = 128, 64$, respectively. Expansion causes the same slow down of nonlinear interactions but the final spectrum is qualitatively different, with run C showing a stronger symmetry around the radial axis. This is because in run C we initially excited modes $k_y > k_x$ while in run E_1 the spectrum

is truly isotropic. All modes at high k_y undergo a kinematic contraction in the Fourier space independently of their k_x extent, so the differences in the final anisotropy arise from the freezing-in of the different initial spectrum.

5. CONCLUSIONS

We studied the anisotropy of turbulence in the solar wind carrying out numerical simulations of the expanding box model for MHD (EBM). We varied both the initial conditions and the expansion rate of our simulations, thus extending recent works on the evolution of turbulence in the solar wind (Dong et al. 2014). To compare with solar wind data we computed how the anisotropy shows up in 2D autocorrelation functions.

We found that if the initial spectrum is already axisymmetric with respect to the mean field, then the spectrum at 1 AU conserves this symmetry and shows up as a 2D-turbulence component, consistent with the above assumption. However, if the initial spectrum is isotropic, then the spectrum at 1 AU is not axisymmetric and the anisotropy is determined by two symmetry axes, the radial axis and the mean-field axis. This is true for a large range of expansion rates and of wavenumbers, suggesting that the mean-field anisotropy is a weak attractor, or in other words that the recovery of homogenous-turbulence properties at small scales is not a universal feature of solar wind turbulence.

We also showed that the assumption of axisymmetry about the mean field, which is often conjectured to hold at small enough scales, may mask the true anisotropy of the magnetic field spectrum. In fact, when the spectrum displays a slab component along the radial, as for isotropic initial conditions, the assumption of axisymmetry about the mean field transforms the anisotropy into an apparent slab component along the mean field.

Thus, on the one hand we confirm earlier results of homogeneous turbulence simulations for the origin of the 2D component (Matthaeus et al. 1990; Ghosh et al. 1998), on the other hand we provide an explanation for the slab component observed in fast streams.

What controls the anisotropy at 1 AU? The B_0 -axisymmetric initial conditions we have used do not only possess the “right” symmetry properties, but also an aspect ratio that is characteristic of strong turbulence (compare the values

of χ in table 1). For reasonable expansion rates, $\epsilon_{\text{end}} \in [0.4, 2]$ (Grappin et al. 1991), turbulence remains strong and its properties are similar to homogenous turbulence. On the contrary, in isotropic initial conditions we excited a large range of field-parallel wavevectors, which makes the cascade weaker. On top of this, expansion slows down the nonlinear interaction due to the kinematic stretching of the plasma. Thus, we have two weakening factors that counteract the natural tendency of MHD turbulence to develop small scales perpendicular to the mean field. In this case, the development of turbulence is more sensitive to the expansion rate and the final anisotropy depends on the expansion symmetry axis, the radial, and on the initial anisotropy.

This leads us to conjecture that slow-wind turbulence is already strongly anisotropic with symmetry axis given by the mean field, and that fast-wind turbulence is more isotropic.

Recall that in fast-wind turbulence a strong correlation between velocity and magnetic fluctuations is observed (high cross-helicity), which results into an additional weakening of the cascade (Verdini et al. 2012a; Perez & Chandran 2013). Such weakening could also be responsible for the formation of the $1/f$ spectrum inside the Alfvénic critical point (Verdini et al. 2012a), which is a characteristic of the fast solar wind (e.g. Bruno & Carbone 2013). Preliminary EBM simulations with initial strong cross helicity and isotropic spectra compare well with turbulence observed in the fast streams (Grappin et al. 1990). Indeed, at 1 AU they have flatter spectra and a higher cross helicity compared to runs with B_0 -axisymmetric initial spectra, suggesting that one needs to account for all the three factors (expansion rate, initial anisotropy, and initial cross helicity) in order to understand the different evolution of turbulence in fast and slow streams.

The so-called Bieber test (Bieber et al. 1996; Saur & Bieber 1999; Smith et al. 2012) that relates spectral and component

anisotropy could be used to further test our conjecture after a proper generalization, i.e., by including the radially-symmetric models of turbulence proposed here.

We conclude by noting that the NASA Solar Probe Plus and ESA Solar Orbiter missions will sample plasma in between 0.1 AU and 0.8 AU. This makes extremely interesting and timely to understand which mechanisms can lead to different initial anisotropies close to the Sun for fast and slow streams. Shell-Reduced-MHD simulations (Verdini et al. 2009, 2012b,a; Verdini & Grappin 2012) are particularly promising, since allow to span 5 decades in wavenumbers and the large parameter space that characterizes slow and fast wind, as well as true Reduced MHD simulations (Perez & Chandran 2013), since they provide more detailed informations on turbulence. Another promising tool is the Accelerating Box Model (Tenerani & Velli 2013), which not only incorporates the acceleration of the solar wind into the EBM but also allows to treat compressible effects, such as parametric instability (e.g. Del Zanna et al. 2014), that are neglected in the above models and may contribute to the acceleration of the solar wind and shape the turbulent spectrum close to the Sun (Suzuki & Inutsuka 2005; Matsumoto & Suzuki 2012).

Acknowledgments We acknowledge R. Bruno, W. H. Matthaeus, and T. K. Suzuki for useful discussions on an earlier version of the manuscript. This work has been done within the LABEX PLAS@PAR project, and received financial state aid managed by the Agence Nationale de la Recherche, as part of the Programme “Investissements d’Avenir” under the reference ANR-11-IDEX-0004-02. HPC resources were provided by CINECA (grant 2015 HP10CVTCYK) and by GENCI-IDRIS (grant 2016 047683).

REFERENCES

- Bieber, J., Wanner, W., & Matthaeus, W. H. 1996, *J. Geophys. Res.*, 101, 2511
- Bruno, R. & Carbone, V. 2013, *Living Reviews in Solar Physics*, 10, 2
- Carbone, V., Malara, F., & Veltri, P. 1995, *J. Geophys. Res.*, 100, 1763
- Chen, C., Mallet, A., Schekochihin, A. A., Horbury, T. S., Wicks, R. T., & Bale, S. 2012, *The Astrophysical Journal*, 758, 120
- Dasso, Milano, L. J., Matthaeus, W. H., & Smith, C. W. 2005, *The Astrophysical Journal Letters*, 635, L181
- Del Zanna, L., Matteini, L., Landi, S., Verdini, A., & Velli, M. 2014, *arXiv.org*, 325810102
- Dmitruk, P. & Gómez, D. O. 1999, *The Astrophysical Journal Letters*, 527, L63
- Dong, Y., Verdini, A., & Grappin, R. 2014, *The Astrophysical Journal*, 793, 118
- Rappazzo F., Velli, M., Einaudi, G., & Dahlburg, R. B. 2007, *The Astrophysical Journal Letters*, 657, L47
- Ghosh, S., Matthaeus, W. H., Roberts, D. A., & Goldstein, M. L. 1998, *J. Geophys. Res.*, 103, 23705
- Grappin, R. 1986, *Physics of Fluids*, 29, 2433
- Grappin, R., Mangeney, A., & Marsch, E. 1990, *J. Geophys. Res.*, 95, 8197
- Grappin, R. & Velli, M. 1996, *J. Geophys. Res.*, 101, 425
- Grappin, R., Velli, M., & Mangeney, A. 1991, *Annales Geophysicae*, 9, 416
- , 1993, *Physical Review Letters*, 70, 2190
- Hamilton, K., Smith, C. W., Vasquez, B. J., & Leamon, R. J. 2008, *J. Geophys. Res.*, 113, 01106
- Matsumoto, T. & Suzuki, T. K. 2012, *The Astrophysical Journal*, 749, 8
- Matthaeus, W. H., Goldstein, M. L., & Roberts, D. A. 1990, *J. Geophys. Res.*, 95, 20673
- Matthaeus, W. H., Servidio, S., Dmitruk, P., Carbone, V., Oughton, S., Wan, M., & Osman, K. 2012, *The Astrophysical Journal*, 750, 103
- Montgomery, D. C. & Turner, L. 1981, *Physics of Fluids*, 24, 825
- Perez, J. C. & Boldyrev, S. 2008, *The Astrophysical Journal*, 672, L61
- Perez, J. C. & Chandran, B. D. G. 2013, *The Astrophysical Journal*, 776, 124
- Saur, J. & Bieber, J. 1999, *J. Geophys. Res.*, 104, 9975
- Shebalin, J. V., Matthaeus, W. H., & Montgomery, D. C. 1983, *Journal of Plasma Physics*, 29, 525
- Smith, C. W., Vasquez, B. J., & Hollweg, J. V. 2012, *The Astrophysical Journal*, 745, 8
- Suzuki, T. K. & Inutsuka, S.-I. 2005, *The Astrophysical Journal Letters*, 632, L49
- Tenerani, A. & Velli, M. 2013, *Journal of Geophysical Research: Space Physics*, 118, 7507
- Verdini, A. & Grappin, R. 2012, *Physical Review Letters*, 109, 025004
- Verdini, A. & Grappin, R. 2015, *The Astrophysical Journal Letters*, 808, L34
- Verdini, A., Grappin, R., Pinto, R. F., & Velli, M. 2012a, *The Astrophysical Journal Letters*, 750, L33
- Verdini, A., Grappin, R., & Velli, M. 2012b, *Astronomy and Astrophysics*, 538, 70
- Verdini, A., Velli, M., & Buchlin, É. 2009, *The Astrophysical Journal Letters*, 700, L39
- Völk, H. J. & Aplers, W. 1973, *Ap&SS*, 20, 267
- Weygand, J. M., Matthaeus, W. H., Dasso, S., & Kivelson, M. G. 2011, *Journal of Geophysical Research*, 116, 8102
- Weygand, J. M., Matthaeus, W. H., Dasso, S., Kivelson, M. G., Kistler, L. M., & Moukikis, C. 2009, *Journal of Geophysical Research*, 114, A07213